In situ architecture and membrane fusion of SARS-CoV-2 Delta variant

Yutong Song[1,2,6], Hangping Yao[3,4,6], Nanping Wu[3,4,6], Zheyuan Zhang[1,2,6], Jialu Xu[1,2,6], Cheng Peng[1,2], Shibo Li[5], Weizheng Kong[1,2], Yong Chen[1,2], Miaojin Zhu[3,4], Jiaqi Wang[1], Danrong Shi[3,4], Chongchong Zhao[1], Xiangyun Lu[3,4], Martín Echavarría Galindo[1] and Sai Li[1,2,7,*]

[1]Beijing Frontier Research Center for Biological Structure & Advanced Innovation Center for Structural Biology, School of Life Sciences, Tsinghua University, Beijing 100084, China

[2]Tsinghua-Peking Center for Life Sciences, Tsinghua University, Beijing 100084, China

[3]State Key Laboratory for Diagnosis and Treatment of Infectious Diseases, The First Affiliated Hospital, Zhejiang University School of Medicine, Hangzhou 310003, Zhejiang Province, China

[4]National Clinical Research Center for Infectious Diseases, The First Affiliated Hospital, Zhejiang University School of Medicine, Hangzhou 310003, Zhejiang Province, China

[5]Department of Infectious Disease, Zhoushan Hospital, Zhejiang University, Zhoushan 316021, Zhejiang Province, China

[6]These authors contributed equally

[7]Lead Contact

* Correspondence: sai@tsinghua.edu.cn (S.L.)

In Brief

Cryo-ET of intact SARS-CoV-2 Delta variant revealed its unique architecture and captured snapshots of its membrane fusion in action.

SUMMARY

Among the current five Variants of Concern, infections caused by the SARS-CoV-2 B.1.617.2 (Delta) variant are often associated with the greatest severity. Despite recent advances on the molecular basis of elevated pathogenicity using recombinant proteins, architecture of intact Delta virions remains veiled. Moreover, the detailed mechanism of S-mediated membrane fusion remains elusive. Here we report the molecular assembly and fusion snapshots of the authentic Delta variant. Envelope invagination and fusion events were frequently observed. Native structures of pre- and postfusion S were determined up to 4.1-Å resolution. Site-specific glycan analysis revealed increased oligomannose-type glycosylation of native Delta S over that of the Wuhan-Hu-1 S. Based on these findings, we proposed a model for S-mediated membrane fusion and a model for the invagination formation.

INTRODUCTION

Despite the progress in global vaccination, the world is suffering from the fourth wave of COVID-19. A major reason for this situation is the continuing emergence of severe acute respiratory syndrome coronavirus 2 (SARS-CoV-2) variants, which impose significant challenges for the administration and development of vaccines and drugs. Among the five Variants of Concern (VOCs) designated by the World Health Organization (WHO), the B.1.617.2 (Delta) variant is one of the most threatening strains. First detected in late 2020, the Delta variant has outcompeted the other variants in India in six months, and has become the globally dominant variant several months later. Epidemiologically, the Delta variant has 97% increased transmissibility (Campbell et al., 2021), causes ~1000 times of viral loads in patients (Li et al., 2022) than the ancestral Wuhan-Hu-1 (WT) strain. In addition, the Delta variant exhibits elevated pathogenicity. Hospitalized patients infected with the Delta variant showed severer symptoms and longer periods of illness (Ong et al., 2021; Twohig et al., 2021). In comparison, Omicron infections is associated with a 70% smaller chances of severe cases (Wolter et al., 2022) and shorter period of illness (Menni et al., 2022) than that of the Delta variant. These phenomena, along with the mutations accumulated in the Delta variant, have validated the descending effectiveness of the current vaccines (Lopez Bernal et al., 2021; McCallum et al., 2021b; Wall et al., 2021) and drugs (Mlcochova et al., 2021). Moreover, recent detection of Delta circulation in wastewater is alerting for its reemergence after Omicron (Yaniv et al., 2022).

Among SARS-CoV-2 proteins, the spike (S) protein is responsible for receptor binding through its receptor binding domain (RBD). Recent structural studies suggest that the recombinant Delta S have improved fitness. They are more likely to adopt the “one RBD up” than the “closed” conformations (Yao et al., 2020; Zhang et al., 2021b), and have much lower binding affinity with the N-terminal domain (NTD)-targeting neutralizing antibodies (NAbs) than the WT S (McCallum et al., 2021b). These changes are orchestrated by a group of characteristic mutations on the Delta S, including T19R, G142D, E156G, Δ157-158, L452R, T478K, D614G, P681R, and D950N. Among these mutations, the T19R, G142D, E156G mutations and Δ157-158 deletions locate at the NTD antigenic supersite (Cerutti et al., 2021; McCallum et al., 2021a). They cause dramatic structural rearrangement, and significantly impair the binding affinity of a large portion of NTD NAbs to the Delta S (McCallum et al., 2021b). L452R and T478K locate at the receptor-binding domain (RBD) of S. L452R has multifunctional roles in reinforcing the S binding with the ACE2 receptor and increasing the

fusion efficacy by 50% (Motozono et al., 2021). D614G, a first prominent mutation detected on S, is adopted by all five VOCs and two variants of interest (VOIs). It alone has been shown to increase the proportion of RBD up conformations among prefusion S, leading to enhanced infectivity (Korber et al., 2020; Zhang et al., 2021a; Zhang et al., 2020). P681R locates at the furin cleavage site between S1/S2 and is unique to the B.1.617 lineage. It has been shown to increase infection via cell surface entry and cause higher pathogenicity by facilitating S1/S2 cleavage and enhancing viral fusogenicity by over 100% (Liu et al., 2021a; Saito et al., 2022). Despite the efforts in elucidating the impact of the Delta variant's mutations on host recognition and immune evasion using recombinant proteins, the architecture of the authentic virus, the in situ structure of its proteins, and distribution of its antigens remain elusive. Using cryo-electron tomography (cryo-ET), we have previously shown the architecture of intact WT SARS-CoV-2 virion, including the native structures and distribution of its S and ribonucleoproteins (RNPs) (Yao et al., 2020). Other cryo-ET studies on infected cells have provided structural insights for the SARS-CoV-2 replication, budding and egressing (Klein et al., 2020; Mendonca et al., 2021; Wolff et al., 2020).

SARS-CoV-2 S is the largest known class-I fusogen. It is believed that angiotensin converting enzyme 2 (ACE2)-binding and following transmembrane serine protease 2 (TMPRSS2) cleavage are both necessary steps for priming the fusion activation (Hoffmann et al., 2020). S of the Delta variant induced the most cell-cell fusion and has the highest fusion dynamics among that of the WT, D614G, Alpha and Beta strains (Rajah et al., 2021). Such syncytia formation may support SARS-CoV-2 replication and transmission, immune evasion, and tissue damage. Furthermore, multinucleated pneumocytes syncytium were present in the lungs of patients with severe COVID-19 symptoms (Bussani et al., 2020; Xu et al., 2020). These in vitro/vivo evidences are suggestive that coronaviral fusogenicity may associate with its pathogenicity (Rajah et al., 2021). Previous cryo-ET studies on the influenza virus-liposome mixture have captured intermediate steps of the hemagglutinin (HA)-mediated fusion (Calder and Rosenthal, 2016; Chlanda et al., 2016; Gui et al., 2016). However, in situ observation of coronavirus S-mediated fusion steps have not been reported yet. Such observation on the Delta variant will be crucial not only in understanding the variant's enhanced fusogenicity, but also providing a molecular basis for SARS-CoV-2 fusion.

Here we combined cryo-ET, subtomogram averaging (STA), single particle analysis (SPA) and mass-spectrometry (MS) for the structural characterizations of intact Delta virions.

The native structure, virion architecture and glycan composition of the Delta variant were compared with those of the WT strain (Ke et al., 2020; Turonova et al., 2020; Yao et al., 2020) and/or the recombinant Delta proteins (McCallum et al., 2021b; Zhang et al., 2021b), and we discovered a dramatically distinctive architecture of the Delta variant. In addition, observation of the virus-virus fusion enabled us to capture key intermediate steps of S-mediated membrane fusion. This allowed detailing of the SARS-CoV-2 fusion process. Our work not only provided a reference of intact Delta virion for the development of vaccines, but also a model for understanding SARS-CoV-2 fusion.

RESULTS

Distinctive features of the Delta variant architecture

The SARS-CoV-2 Delta variant (hCoV-19/Hangzhou/ZJU-12/2021) was collected on May, 2021 from the sputum samples of a COVID-19 patient in Zhoushan, Zhejiang province, and was the first isolated Delta variant in China (GISAID: EPI_ISL_3127444.2). The strain lacks the E156G and Δ157-158 mutations on S. Virions were propagated in either Vero or Calu-3 cells in a BSL-3 laboratory and were fixed with paraformaldehyde (PFA) prior to concentration and cryo-electron microscopy (cryo-EM) analysis. The fixation is reported to have minor effects on protein structures up to subnanometer resolution and the overall assembly (Li et al., 2016; Wan et al., 2017; Yao et al., 2020). To avoid crushing the virions against the tube bottom during ultracentrifugation, we pelleted the virions onto the interface between 30% and 50% sucrose cushion.

With cryo-ET, we have imaged and reconstructed 1,032 Delta virions as volumetric data (table S1). The most distinctive feature of the Delta versus WT viral architecture is the presence of a large envelope concavity in the majority of virions (Figures 1A-1C and 1E). The concavity, which is commonly seen in cell biology but hardly reported on enveloped viruses, is designated here as “invagination”. To validate that the invagination did not rise from cell lines that were used for virus propagation, or ultracentrifugation, we have imaged unconcentrated Delta virions from the infected Vero-cell supernatant (Figure S1A), concentrated Vero cell-propagated Delta virions (Figure 1A) and concentrated Calu-3 cell-propagated Delta virions (Figure S1B). As a result, invagination is common in all conditions, but absent in Vero cell-propagated WT virions that were concentrated same as the above conditions (Figure S1C). For the convenience of description, key parts of the invaginated virions are named as in (Figure 1F).

Scrutiny of the invaginated virions has revealed common features. First, the virus is characterized by either a balloon-shaped, or a cylindrical invagination (Figure 1D). These invaginations have an average depth of 45.8 nm, and connect the virion exterior through a neck with an average diameter of 7.6 nm (Figure S2E). Despite the invagination, Delta virions have similar volume within the viral lumen compared to WT virions (Figure S2F). Second, S distribute only on the virion exterior, while there is no appearance of S inside the invagination lumen. Furthermore, the neck region is often populated with S (Figures S2A-S2D). Third, the dramatic luminal reorganization is accompanied by the change of viral RNP assembly. In WT virions, bead-like RNPs are often individually discernable, relatively homogeneously distributed, and hexagonally assembled on the cytoplasmic surface of the envelope (Yao et al., 2020). While in invaginated Delta virions, the majority of RNPs form a dense layer wrapping around the invaginated envelope and leave the rest of viral lumen empty (Figures 1A-1C). Last, the viral envelope neighboring the invagination bottom (referred to as viral bottom) is largely devoid of RNPs and S, or sometimes even broken. Of the 721 invaginated virions, 216 have broken viral bottom. Lipid-bilayer densities from envelopes of the WT virions, Delta viral bottom and Delta invagination lumen were subtomogram averaged for comparison, revealing relatively thinner lipid bilayers on the Delta viral bottom (Figure S2G). This suggests that the area may have been subjected to extensive tension (Reddy et al., 2012).

Membrane fusion of Delta virions

Another distinctive feature of the Delta verses WT virions is the frequent observations of S-involved membrane insertion, dimpling or pinching of membranes in the tomograms, reminiscent of typical intermediate steps of class-I fusogen mediated membrane fusion (Li, 2022). We sorted these observations into six sequential stages of a fusion process (Figures 2A, 2B, and S3), and further characterized these steps to illustrate the SARS-CoV-2 fusion mechanism (Figures 2C and 2D): 1) Two envelopes connected by a long, thin and straight bar density, which has an average length of 26.3 nm, 34% longer than the length of a postfusion S (Figure S3A). This is denoted S2-mediated bridging. 2) Two envelopes connected by long, thin but kinked bars, which consist of a shorter rear arm (average length: 8.9 nm) and longer forearm (average length: 15.4 nm) linked by an elbow region, with an average kink angle of 143° (Figure S3B). This is denoted S-mediated dimpling. 3) Two “kissing” envelopes featuring membranes in primary contact. Thin, straight bars were often seen surrounding the contact area. 15 bars from 8 independent events were averaged by STA, which reconstructed a 21.7 nm long spike inserted between two envelopes. Fitting the spike with a postfusion S structure

(PDB:6XRA) suggests that it is close to the postfusion form (Figure S3C). Segmentation of one event revealed a group of six spikes radiating away from the membrane contact point, forming a star-shaped pattern. This is similar to influenza HA mediated pinching (Calder and Rosenthal, 2016). During the three steps, RNPs remain attached to the cytoplasmic side of the membrane underlying the participating spikes, suggesting that the N-associated M-assembly has not become disrupted yet (Lu et al., 2021). 4) Two envelopes forming a tightly docked interface. The interface is formed by two bilayers, as measured by the density profile, and can extend as wide as 36 nm. At least one involved virion is distorted, with its membrane pulled away from its RNPs towards the interface, suggesting M-assembly has become disrupted. 5) Two envelopes with their membranes forming a single-bilayer interface, as measured by the density profile. This is denoted hemifusion. 6) One large virion harboring S on the envelope while containing two sets of RNPs inside. This is denoted fusion completion. The above phenomena were very rare or absent from our previous data of WT SARS-CoV-2 (Yao et al., 2020).

The molecular landscape of S on intact SARS-CoV-2 Delta virions

In total we identified 22,695 prefusion S and 2,810 postfusion S from the tomograms. The virion has an average of 32 ± 12 S, 24 ± 10 being prefusion S and 7 ± 4 being postfusion S (Figure 3D). STA and classification revealed that 36.4% prefusion S adopt the closed conformation, and 63.6% adopt the one RBD up conformation. The two prefusion conformations, together with the postfusion conformation, were reconstructed to 9.8 Å, 13.0 Å and 11.9 Å resolution (Figures 3A, 3C, and S4). At this resolution, no obvious difference was observed in the overall architecture of native S from that of the WT strain (Yao et al., 2020). Statistics of refined orientations of the prefusion S suggested freedom of S rotating around their stalks outside the envelope, with a mean tilting angle of 49° (std: 21.5°) relative to the normal axis of the envelope (Figure 3B). For invaginated virions, S tend to accumulate around the neck area (Figure 3E).

The native structure and glycan compositions of S in the prefusion conformation

To gain further insights on the S structure *in situ*, a SPA approach was applied for the imaging and structural analysis of the full-length S-trimers (Figure S5 and Table S2). Spikes were identified directly from the periphery of intact Delta virions (Figure 4B), and subsequent SPA revealed a 4.1-Å resolution structure of prefusion S in the closed conformation (Figures 4A and S6). Despite the missing E156G and Δ157-158 mutations in our sample (Figure 4D), the

overall architecture of the native Delta S is similar to that of the recombinant Delta S (Zhang et al., 2021b) and the native D614G S (Ke et al., 2020) in the closed conformation, except for the weaker density of the receptor binding motif (RBM), which suggests that this region is more dynamic *in situ*. Compared to the recombinant WT S (Cai et al., 2020), a clockwise, outward rotation of NTD is evident on the native Delta S (Figure S7A).

The T19R mutation is known to eliminate the N17 glycan. Among the remaining 21 N-linked glycosylation sites, densities of 16 glycans are visible on the native structure, of which N282, N343, N717, N801, N1074, N1098 and N1134 are best resolved. N343, which has been proposed to have a gating role and facilitate RBD opening (Sztain et al., 2021), forms a bulky bridge between the RBD and the neighboring RBM (Figure S7B). Among the unsolved or poorly solved sites, N74 locates in an unsolved loop region. N149 locates on the periphery of NTD, while N1158, N1173 and N1194 locate on the stem. We further performed a site-specific glycan analysis of the native S by resolving the virus sample on SDS-PAGE, and analyzing the bands corresponding to S1 and S2 with mass spectrometry (MS). Of the 19 glycans detected and analyzed, the native Delta S glycans contain more oligomannose-type glycosylation compared to the native WT S glycans (Allen et al., 2021; Yao et al., 2020) (Figure 4C). N149 and N1158 are missing in both the cryo-EM structure and MS results.

DISCUSSION

In this work, the *in situ* analysis of S provided molecular basis for the enhanced infectivity of the Delta variant than the WT strain. The Delta variant harbors 23.1% more S than the WT strain. Given their similar average diameters, the population density of S is higher on the Delta variant. Moreover, the native Delta S are found to be more dynamic than those of the WT strain from various structural aspects. First, a 18% larger proportion of prefusion S adopted the one RBD up conformation. Second, on average ~600% more postfusion S were found on each virion. Third, the Delta prefusion S rotate more vigorously around their stalks on the envelope. Last, the weak RBM densities on native Delta S suggest that this region is more dynamic and likely prone to receptor binding. Such enhanced dynamics from various structural aspects have contributed to an enhanced overall effect of receptor-binding and membrane fusion of the Delta variant, and may be attributed to mutations such as L452R, D614G and P681R. In terms of glycan composition, there is a greater proportion of oligomannose on Delta S than that on WT S. This implicates that the significantly higher viral production of Delta variant in the cell outspeeds the capacity of the cell to process the large number of glycan sites present on S in its Golgi. The increased oligomannose on Delta S may also facilitate virus-host cell attachment

and viral entry through oligomannose-GlcNAc glycan-glycan interactions, as was observed on HIV (Spillings et al., 2022). The structure, glycan analysis and statistics of S on the virion also provide in situ profiles of effective antigens, which is an important reference for vaccine development.

An opportunity to understand the SARS-CoV-2 fusion mechanism rises from the fusion events frequently observed in our data, the majority of which are between two virions. For the virus-liposome fusion, where the unsupported liposome membrane is clearly pulled towards the virus (Gui et al., 2016), it is unambiguous to distinguish the viral membrane (M_V) from the target membrane (M_T). However, this is not obvious for the virus-virus fusion, since both sides of the membranes are supported by M- and RNP-lattices. Comparison of S2 in its prefusion (PDB:7SBK) and postfusion (PDB:6XRA) conformations suggests that the longer arm of the dimpling S2 comprises the fusion peptide (FP), the heptad repeat 1 (HR1) and the central helix (CH) domain; and the shorter arm comprises the heptad repeat 2 (HR2) and the transmembrane anchor (TM) domain. The two arms are linked by an elbow region comprised of a relatively rigid β-rich module (residues 1035-1140) (Figure 5A). These identifications are supported by the averaged length and angles measured from the dimpling S2 (Figures S3A and S3B), and helped us determined the shorter-arm-attached membrane to be M_V and the other to be M_T. As fusion proceeds, at least one involving virion becomes distorted, with its membrane pulled away from its RNPs. This membrane area is often devoid of spikes, suggesting that the pulling has possibly disrupted the M-lattice, whose interaction with S and N plays key roles in viral assembly (Bracquemond and Muriaux, 2021). Among the six steps of fusion activities present in the tomograms, the pinching and tightly docked interface were the most frequently observed events, suggesting that these steps are metastable. The hemifusion was relatively rare, which reflects its transient nature. These observations are in agreement with the Influenza A virus hemagglutinin (HA) mediate fusion (Calder and Rosenthal, 2016; Chlanda et al., 2016; Gui et al., 2016). Upon these observations, we proposed a model for the SARS-CoV-2 S-mediated spontaneous fusion (Figure 5A). To begin with, S1 spontaneously sheds, which is facilitated by mutations such as L452R and P681R. Then HR1 unfolds and inserts FP into the target membrane, forming an extended intermediate. The membrane-embedded M-lattice and the M-affiliated RNP-lattices remain intact at this stage. The FP-HR1-CH region then refolds around the β-module towards the HR2-TM region, pinching the viral and target membrane. Since this stage, the M-lattice has become disrupted and the RNP-lattice has disassembled from the viral membrane. After going through the tightly docked and hemifusion transitions, the pinched

membranes finally fuse. The exhausted S2 eventually adopts a postfusion conformation. A necessary condition for the virus-virus fusion is the proximity of virions. Since our virions were fixed prior to concentration, we argue that the fusion most likely occurred during virus budding or egressing. In both steps, the assembling or assembled SARS-CoV-2 virions can accumulate in small cellular compartments, such as ER-Golgi intermediate compartment (ERGIC) (Klein et al., 2020; Mendonca et al., 2021) or lysosomes (Ghosh et al., 2020; Mendonca et al., 2021).

The unexpected invagination is another unique feature of Delta variant among enveloped viruses. Although we cannot fully exclude the possibility that mutations on N are responsible for the invagination (Syed et al., 2021), evidences in our data support a S-mediated process for the invagination formation in Delta virions (Figure 5B). In this model, the invagination is initiated by S-mediated spontaneous self-fusion on the envelope. Shedding of S1 allows the insertion of S2 fusion peptide into the underlying membrane. The process of S2 refolding into postfusion form wrinkles the membrane and thus forms a dimple. As the neighboring membrane and S are pulled towards the dimple, more prefusion S join the fusion site, fusing the dimple into an intraviral vesicle, or in the majority of cases, enlarging the dimple into an invagination. During the invagination formation, the viral bottom has endured substantial tension, which disrupts the M-M assembly or in some cases breaks the viral envelope. The disruption on the viral bottom reorganizes the local RNPs into a layer wrapping around the invaginated membrane. Finally, the transformed postfusion S stays at the neck region. This model is supported by common features observed on the Delta virions, together with previous studies on S and N: 1) lying of prefusion S on the viral envelope (Figure S8A); 2) accumulation of S around the neck region (Figures 3E and S8E); 3) occasional observations of pre- and postfusion S in the middle of the neck, and comparable neck diameter to the length of S (Figures S8B and S8C); 4) absence of S inside the invagination (Figures S8E and S8F); 5) RNPs wrapping around the invagination (Figures 1A-1C); 6) observation of vesicles in the viral lumen (Figure S8D); 7) frequent observations of bald (Figure S8E) or broken (Figure S8F) viral bottom devoid of both RNPs and S, together with thinner lipid bilayers on the viral bottom (Figure S2G), suggesting that the area have been subjected to extensive tension, which may disrupt the M-assembly across this area; 8) Delta mutations such as L452R and P681R have been shown to increase the chance of S1/S2 cleavage and significantly enhance fusogenicity (Liu et al., 2021a; Motozono et al., 2021; Saito et al., 2022), which may facilitate spontaneous fusion. The unique architecture of invaginated virions may be advantageous for enhancing viral

infectivity. The invagination concentrates S towards one hemisphere of the virion, which could be favorable for virus attachment to the host cell.

In conclusion, the larger proportion of S in RBD up conformations, the aggressively tilting S, the significantly increased number of postfusion S, virus-virus fusion and invagination observed in our data have provided molecular basis for the exceptional fusogenicity of Delta variant. These evidences collectively suggest that Delta S are tuned in a more unstable state, attenuating its dependency on ACE2 or TMPRSS2 for fusion. Indeed, cell-cell fusion can be induced either by Delta S on cells with no exogenous ACE2 (Zhang et al., 2021b) or by D614G/P681R S on cells with no exogenous TMPRSS2 (Saito et al., 2022). This is alarming for strategies that tried to use TMPRSS2 inhibitor to block virus entry (Gunst et al., 2021). Furthermore, comparison of the Delta and Omicron variants with the WT strain suggested that the fusogenicity of a SARS-CoV-2 strain may associate with its pathogenicity. Thus, the prominent fusogenicity may explain for the greater severity and unusual symptoms of Delta infections (Saito et al., 2022; Suzuki et al., 2022), and is alerting for future variants that may carry similar fusogenicity-enhancing mutations, such as the newly emerged L452R-carrying Omicron BA.4/BA.5 subvariants.

ACKNOWLEDGMENTS

S.L. thanks Tsinghua University for providing a Start-up fund, the Tsinghua University Branch of China National Center for Protein Sciences (Beijing) for the cryo-EM facility and the computational facility support, and Dr. Fan Yang, Liao Zhang for technical support. We thank Dr. Jianlin Lei in the cryo-EM Facility, Dr. Lingpeng Cheng in the Cryo-EM Structural Analysis Facility, and Dr. Haiteng Deng in the Proteinomics Facility at Technology Center for Protein Sciences, Tsinghua University, for cryo-EM data collection, structural analysis and protein MS; Haibo Wu, Changzhong Jin and Zhigang Wu in the State Key Laboratory for Diagnosis and Treatment of Infectious Diseases, The First Affiliated Hospital, Zhejiang University School of Medicine, for virus fixation and biosafety validation. We thank the computational facility support on the cluster of Bio-Computing Platform (Tsinghua University Branch of China National Center for Protein Sciences Beijing). We are in debt to Dr. Hongwei Wang and Dr. Nieng Yan for providing critical advices. **FUNDING:** This work was supported in part from Tsinghua University Spring Breeze Fund #2021Z99CFZ004 (SL), National Natural Science Foundation of China #32171195 (SL), Zhejiang Provincial Key Research and Development Program #2021C03043 (HY), and National Key Research and Development Program in China #2021YFC2301200 (HY).

AUTHOR CONTRIBUTIONS

S.L. conceptualized the models and supervised the project. Shibo L. isolated virus and conducted clinical diagnosis. H.Y., N.W., M.Z., D.S., and X.L. propagated and fixed the virus sample. YS purified the virus, prepared EM grids and collected cryo-ET data. Y.S., Z.Z., C.P., W.K., J.W., Y.C. and S.L. analyzed cryo-ET data. Cryo-EM data collection and analysis: J.X, Y.S and M.E.G. collected and analyzed cryo-EM data. Z.Z. and Y.S. performed the statistical analysis. MS data collection and analysis: Y.S. and C.Z. collected and analyzed MS data. S.L. wrote the original draft. W.K., C.P., Y.S., H.Y. and S.L. reviewed and edited the manuscript. Y.S., Z.Z., J.X., and C.P. prepared the figures. S.L., H.Y., and N.W. acquired funding and administrated the protect.

DECLARATION OF INTERESTS

The authors declare no competing interests.

REFERENCES

Allen, J.D., Chawla, H., Samsudin, F., Zuzic, L., Shivgan, A.T., Watanabe, Y., He, W.T., Callaghan, S., Song, G., Yong, P., et al. (2021). Site-specific steric control of SARS-CoV-2 spike glycosylation. Biochemistry *60*, 2153-2169. 10.1021/acs.biochem.1c00279.

Bepler, T., Morin, A., Rapp, M., Brasch, J., Shapiro, L., Noble, A.J., and Berger, B. (2019). Positive-unlabeled convolutional neural networks for particle picking in cryo-electron micrographs. Nat. methods *16*, 1153-1160. 10.1038/s41592-019-0575-8.

Berg, S., Kutra, D., Kroeger, T., Straehle, C.N., Kausler, B.X., Haubold, C., Schiegg, M., Ales, J., Beier, T., Rudy, M., et al. (2019). ilastik: interactive machine learning for (bio)image analysis. Nat. methods *16*, 1226-1232. 10.1038/s41592-019-0582-9.

Bracquemond, D., and Muriaux, D. (2021). Betacoronavirus assembly: clues and perspectives for elucidating SARS-CoV-2 particle formation and egress. mBio *12*, e0237121. 10.1128/mBio.02371-21.

Bussani, R., Schneider, E., Zentilin, L., Collesi, C., Ali, H., Braga, L., Volpe, M.C., Colliva, A., Zanconati, F., Berlot, G., et al. (2020). Persistence of viral RNA, pneumocyte syncytia and thrombosis are hallmarks of advanced COVID-19 pathology. EBioMedicine *61*, 103104. 10.1016/j.ebiom.2020.103104.

Cai, Y., Zhang, J., Xiao, T., Peng, H., Sterling, S.M., Walsh, R.M., Jr., Rawson, S., Rits-Volloch, S., and Chen, B. (2020). Distinct conformational states of SARS-CoV-2 spike protein. Science *369*, 1586-1592. 10.1126/science.abd4251.

Calder, L.J., and Rosenthal, P.B. (2016). Cryomicroscopy provides structural snapshots of influenza virus membrane fusion. Nat. Struct. Mol. Biol. *23*, 853-858. 10.1038/nsmb.3271.

Campbell, F., Archer, B., Laurenson-Schafer, H., Jinnai, Y., Konings, F., Batra, N., Pavlin, B., Vandemaele, K., Van Kerkhove, M.D., Jombart, T., et al. (2021). Increased transmissibility and global spread of SARS-CoV-2 variants of concern as at June 2021. Euro surveill. *26*. 10.2807/1560-7917.ES.2021.26.24.2100509.

Castano-Diez, D., Kudryashev, M., Arheit, M., and Stahlberg, H. (2012). Dynamo: a flexible, user-friendly development tool for subtomogram averaging of cryo-EM data in high-performance computing environments. J. Struct. Biol. *178*, 139-151. 10.1016/j.jsb.2011.12.017.

Cerutti, G., Guo, Y., Zhou, T., Gorman, J., Lee, M., Rapp, M., Reddem, E.R., Yu, J., Bahna, F., Bimela, J., et al. (2021). Potent SARS-CoV-2 neutralizing antibodies directed against spike N-terminal domain target a single supersite. Cell Host Microbe *29*, 819-833 e817. 10.1016/j.chom.2021.03.005.

Chlanda, P., Mekhedov, E., Waters, H., Schwartz, C.L., Fischer, E.R., Ryham, R.J., Cohen, F.S., Blank, P.S., and Zimmerberg, J. (2016). The hemifusion structure induced by influenza virus haemagglutinin is determined by physical properties of the target membranes. Nat. microbiol. *1*, 16050. 10.1038/nmicrobiol.2016.50.

Fedorov, A., Beichel, R., Kalpathy-Cramer, J., Finet, J., Fillion-Robin, J.C., Pujol, S., Bauer, C., Jennings, D., Fennessy, F., Sonka, M., et al. (2012). 3D Slicer as an image computing platform for the Quantitative Imaging Network. Magn. Reson. Imaging *30*, 1323-1341.

Ghosh, S., Dellibovi-Ragheb, T.A., Kerviel, A., Pak, E., Qiu, Q., Fisher, M., Takvorian, P.M., Bleck, C., Hsu, V.W., Fehr, A.R., et al. (2020). Beta-coronaviruses use lysosomes for egress instead of the biosynthetic secretory pathway. Cell *183*, 1520-1535 e14. 10.1016/j.cell.2020.10.039.

Gui, L., Ebner, J.L., Mileant, A., Williams, J.A., and Lee, K.K. (2016). Visualization and sequencing of membrane remodeling leading to influenza virus fusion. J. Virol. *90*, 6948-6962. 10.1128/JVI.00240-16.

Gunst, J.D., Staerke, N.B., Pahus, M.H., Kristensen, L.H., Bodilsen, J., Lohse, N., Dalgaard, L.S., Bronnum, D., Frobert, O., Honge, B., et al. (2021). Efficacy of the TMPRSS2 inhibitor camostat mesilate in patients hospitalized with Covid-19-a double-blind randomized controlled trial. EClinicalMedicine *35*, 100849. 10.1016/j.eclinm.2021.100849.

Hagen, W.J.H., Wan, W., and Briggs, J.A.G. (2017). Implementation of a cryo-electron tomography tilt-scheme optimized for high resolution subtomogram averaging. J. Struct. Biol. *197*, 191-198. 10.1016/j.jsb.2016.06.007.

Hoffmann, M., Kleine-Weber, H., Schroeder, S., Kruger, N., Herrler, T., Erichsen, S., Schiergens, T.S., Herrler, G., Wu, N.H., Nitsche, A., et al. (2020). SARS-CoV-2 cell entry depends on ACE2 and TMPRSS2 and is blocked by a clinically proven protease inhibitor. Cell *181*, 271-280 e8. 10.1016/j.cell.2020.02.052.

Ke, Z., Oton, J., Qu, K., Cortese, M., Zila, V., McKeane, L., Nakane, T., Zivanov, J., Neufeldt, C.J., Cerikan, B., et al. (2020). Structures and distributions of SARS-CoV-2 spike proteins on intact virions. Nature *588*, 498-502. 10.1038/s41586-020-2665-2.

Klein, S., Cortese, M., Winter, S.L., Wachsmuth-Melm, M., Neufeldt, C.J., Cerikan, B., Stanifer, M.L., Boulant, S., Bartenschlager, R., and Chlanda, P. (2020). SARS-CoV-2 structure and replication characterized by in situ cryo-electron tomography. Nat. Commun. *11*, 5885. 10.1038/s41467-020-19619-7.

Korber, B., Fischer, W.M., Gnanakaran, S., Yoon, H., Theiler, J., Abfalterer, W., Hengartner, N., Giorgi, E.E., Bhattacharya, T., Foley, B., et al. (2020). Tracking Changes in SARS-CoV-2 Spike: Evidence that D614G Increases Infectivity of the COVID-19 Virus. Cell *182*, 812-827 e19. 10.1016/j.cell.2020.06.043.

Kremer, J.R., Mastronarde, D.N., and McIntosh, J.R. (1996). Computer visualization of three-dimensional image data using IMOD. J. Struct. Biol. *116*, 71-76. 10.1006/jsbi.1996.0013.

Lei, J., and Frank, J. (2005). Automated acquisition of cryo-electron micrographs for single particle reconstruction on an FEI Tecnai electron microscope. J. Struct. Biol. *150*, 69-80. 10.1016/j.jsb.2005.01.002.

Li, B., Deng, A., Li, K., Hu, Y., Li, Z., Shi, Y., Xiong, Q., Liu, Z., Guo, Q., Zou, L., et al. (2022). Viral infection and transmission in a large, well-traced outbreak caused by the SARS-CoV-2 Delta variant. Nat. Commun. *13*, 460. 10.1038/s41467-022-28089-y.

Li, S. (2022). Cryo-electron tomography of enveloped viruses. Trends. Biochem. Sci. *47*, 173-186. 10.1016/j.tibs.2021.08.005.

Li, S., Sun, Z., Pryce, R., Parsy, M.L., Fehling, S.K., Schlie, K., Siebert, C.A., Garten, W., Bowden, T.A., Strecker, T., and Huiskonen, J.T. (2016). Acidic pH-Induced Conformations and LAMP1 Binding of the Lassa Virus Glycoprotein Spike. PLoS. Pathog. *12*, e1005418. 10.1371/journal.ppat.1005418.

Li, X., Mooney, P., Zheng, S., Booth, C.R., Braunfeld, M.B., Gubbens, S., Agard, D.A., and Cheng, Y. (2013). Electron counting and beam-induced motion correction enable near-atomic-resolution single-particle cryo-EM. Nat. methods *10*, 584-590. 10.1038/nmeth.2472.

Liu, Y., Liu, J., Johnson, B.A., Xia, H., Ku, Z., Schindewolf, C., Widen, S.G., An, Z., Weaver, S.C., Menachery, V.D., et al. (2021a). Delta spike P681R mutation enhances SARS-CoV-2 fitness over Alpha variant. bioRxiv, https://www.biorxiv.org/content/10.1101/2021.08.12.456173v3 (2021).

Liu, Y.-T., Zhang, H., Wang, H., Tao, C.-L., Bi, G.-Q., and Zhou, Z.H. (2021b). Isotropic Reconstruction of Electron Tomograms with Deep Learning. bioRxiv, https://www.biorxiv.org/content/10.1101/2021.07.17.452128v1 (2021).

Lopez Bernal, J., Andrews, N., Gower, C., Gallagher, E., Simmons, R., Thelwall, S., Stowe, J., Tessier, E., Groves, N., Dabrera, G., et al. (2021). Effectiveness of Covid-19 Vaccines against the B.1.617.2 (Delta) Variant. N. Engl. J. Med. *385*, 585-594. 10.1056/NEJMoa2108891.

Lu, S., Ye, Q., Singh, D., Cao, Y., Diedrich, J.K., Yates, J.R., 3rd, Villa, E., Cleveland, D.W., and Corbett, K.D. (2021). The SARS-CoV-2 nucleocapsid phosphoprotein forms mutually exclusive condensates with RNA and the membrane-associated M protein. Nat. Commun. *12*, 502. 10.1038/s41467-020-20768-y.

Mastronarde, D.N. (2005). Automated electron microscope tomography using robust prediction of specimen movements. J. Struct. Biol. *152*, 36-51. 10.1016/j.jsb.2005.07.007.

McCallum, M., De Marco, A., Lempp, F.A., Tortorici, M.A., Pinto, D., Walls, A.C., Beltramello, M., Chen, A., Liu, Z., Zatta, F., et al. (2021a). N-terminal domain antigenic mapping reveals a site of vulnerability for SARS-CoV-2. Cell *184*, 2332-2347 e16. 10.1016/j.cell.2021.03.028.

McCallum, M., Walls, A.C., Sprouse, K.R., Bowen, J.E., Rosen, L.E., Dang, H.V., De Marco, A., Franko, N., Tilles, S.W., Logue, J., et al. (2021b). Molecular basis of immune evasion by the Delta and Kappa SARS-CoV-2 variants. Science *374*, 1621-1626. 10.1126/science.abl8506.

Mendonca, L., Howe, A., Gilchrist, J.B., Sheng, Y., Sun, D., Knight, M.L., Zanetti-Domingues, L.C., Bateman, B., Krebs, A.S., Chen, L., et al. (2021). Correlative multi-scale cryo-imaging unveils SARS-CoV-2 assembly and egress. Nat. Commun. *12*, 4629. 10.1038/s41467-021-24887-y.

Menni, C., Valdes, A.M., Polidori, L., Antonelli, M., Penamakuri, S., Nogal, A., Louca, P., May, A., Figueiredo, J.C., Hu, C., et al. (2022). Symptom prevalence, duration, and risk of hospital admission in individuals infected with SARS-CoV-2 during periods of omicron and delta variant dominance: a prospective observational study from the ZOE COVID Study. Lancet *2022*, 10.1016/S0140-6736(22)00327-0.

Mlcochova, P., Kemp, S.A., Dhar, M.S., Papa, G., Meng, B., Ferreira, I., Datir, R., Collier, D.A., Albecka, A., Singh, S., et al. (2021). SARS-CoV-2 B.1.617.2 Delta variant replication and immune evasion. Nature *599*, 114-119. 10.1038/s41586-021-03944-y.

Motozono, C., Toyoda, M., Zahradnik, J., Saito, A., Nasser, H., Tan, T.S., Ngare, I., Kimura, I., Uriu, K., Kosugi, Y., et al. (2021). SARS-CoV-2 spike L452R variant evades cellular immunity and increases infectivity. Cell Host Microbe *29*, 1124-1136 e11. 10.1016/j.chom.2021.06.006.

Ong, S.W.X., Chiew, C.J., Ang, L.W., Mak, T.M., Cui, L., Toh, M., Lim, Y.D., Lee, P.H., Lee, T.H., Chia, P.Y., et al. (2021). Clinical and virological features of SARS-CoV-2 variants of concern: a retrospective cohort study comparing B.1.1.7 (Alpha), B.1.315 (Beta), and B.1.617.2 (Delta). Clin. Infect. Dis. *2021*, 10.1093/cid/ciab721.

Perez-Riverol, Y., Bai, J., Bandla, C., Garcia-Seisdedos, D., Hewapathirana, S., Kamatchinathan, S., Kundu, D.J., Prakash, A., Frericks-Zipper, A., Eisenacher, M., et al. (2022). The PRIDE database resources in 2022: a hub for mass spectrometry-based proteomics evidences. Nucleic Acids Res. *50*, D543-D552. 10.1093/nar/gkab1038.

Rajah, M.M., Hubert, M., Bishop, E., Saunders, N., Robinot, R., Grzelak, L., Planas, D., Dufloo, J., Gellenoncourt, S., Bongers, A., et al. (2021). SARS-CoV-2 Alpha, Beta, and Delta variants display enhanced Spike-mediated syncytia formation. EMBO. J. *40*, e108944. 10.15252/embj.2021108944.

Reddy, A.S., Warshaviak, D.T., and Chachisvilis, M. (2012). Effect of membrane tension on the physical properties of DOPC lipid bilayer membrane. Biochi. Biophys. Acta *1818*, 2271-2281. 10.1016/j.bbamem.2012.05.006.

Rohou, A., and Grigorieff, N. (2015). CTFFIND4: Fast and accurate defocus estimation from electron micrographs. J. Struct. Biol. *192*, 216-221. 10.1016/j.jsb.2015.08.008.

Saito, A., Irie, T., Suzuki, R., Maemura, T., Nasser, H., Uriu, K., Kosugi, Y., Shirakawa, K., Sadamasu, K., Kimura, I., et al. (2022). Enhanced fusogenicity and pathogenicity of SARS-CoV-2 Delta P681R mutation. Nature *602*, 300-306. 10.1038/s41586-021-04266-9.

Scheres, S.H. (2012). RELION: implementation of a Bayesian approach to cryo-EM structure determination. J. Struct. Biol. *180*, 519-530. 10.1016/j.jsb.2012.09.006.

Spillings, B.L., Day, C.J., Garcia-Minambres, A., Aggarwal, A., Condon, N.D., Haselhorst, T., Purcell, D.F.J., Turville, S.G., Stow, J.L., Jennings, M.P., and Mak, J. (2022). Host glycocalyx captures HIV proximal to the cell surface via oligomannose-GlcNAc glycan-glycan interactions to support viral entry. Cell Rep. *38*, 110296. 10.1016/j.celrep.2022.110296.

Suzuki, R., Yamasoba, D., Kimura, I., Wang, L., Kishimoto, M., Ito, J., Morioka, Y., Nao, N., Nasser, H., Uriu, K., et al. (2022). Attenuated fusogenicity and pathogenicity of SARS-CoV-2 Omicron variant. Nature *603*, 700-705. 10.1038/s41586-022-04462-1.

Syed, A.M., Taha, T.Y., Tabata, T., Chen, I.P., Ciling, A., Khalid, M.M., Sreekumar, B., Chen, P.Y., Hayashi, J.M., Soczek, K.M., et al. (2021). Rapid assessment of SARS-CoV-2-evolved variants using virus-like particles. Science 374, 1626-1632. 10.1126/science.abl6184.

Sztain, T., Ahn, S.H., Bogetti, A.T., Casalino, L., Goldsmith, J.A., Seitz, E., McCool, R.S., Kearns, F.L., Acosta-Reyes, F., Maji, S., et al. (2021). A glycan gate controls opening of the SARS-CoV-2 spike protein. Nat. Chem. *13*, 963-968. 10.1038/s41557-021-00758-3.

Tegunov, D., and Cramer, P. (2019). Real-time cryo-electron microscopy data preprocessing with Warp. Nat. methods *16*, 1146-1152. 10.1038/s41592-019-0580-y.

Turonova, B., Schur, F.K.M., Wan, W., and Briggs, J.A.G. (2017). Efficient 3D-CTF correction for cryo-electron tomography using NovaCTF improves subtomogram averaging resolution to 3.4 Å . J. Struct. Biol. *199*, 187-195. 10.1016/j.jsb.2017.07.007.

Turonova, B., Sikora, M., Schurmann, C., Hagen, W.J.H., Welsch, S., Blanc, F.E.C., von Bulow, S., Gecht, M., Bagola, K., Horner, C., et al. (2020). In situ structural analysis of SARS-CoV-2 spike reveals flexibility mediated by three hinges. Science *370*, 203-208. 10.1126/science.abd5223.

Twohig, K.A., Nyberg, T., Zaidi, A., Thelwall, S., Sinnathamby, M.A., Aliabadi, S., Seaman, S.R., Harris, R.J., Hope, R., Lopez-Bernal, J., et al. (2021). Hospital admission and emergency care attendance risk for SARS-CoV-2 delta (B.1.617.2) compared with alpha (B.1.1.7) variants of concern: a cohort study. Lancet Infect. Dis. *22*, 10.1016/s1473-3099(21)00475-8.

Wall, E.C., Wu, M., Harvey, R., Kelly, G., Warchal, S., Sawyer, C., Daniels, R., Hobson, P., Hatipoglu, E., Ngai, Y., et al. (2021). Neutralising antibody activity against SARS-CoV-2 VOCs B.1.617.2 and B.1.351 by BNT162b2 vaccination. Lancet *397*, 2331-2333. 10.1016/s0140-6736(21)01290-3.

Walls, A.C., Park, Y.J., Tortorici, M.A., Wall, A., McGuire, A.T., and Veesler, D. (2020). Structure, Function, and Antigenicity of the SARS-CoV-2 Spike Glycoprotein. Cell *181*, 281-292 e6. 10.1016/j.cell.2020.02.058.

Wan, W., Kolesnikova, L., Clarke, M., Koehler, A., Noda, T., Becker, S., and Briggs, J.A.G. (2017). Structure and assembly of the Ebola virus nucleocapsid. Nature *551*, 394-397. 10.1038/nature24490.

Wolff, G., Limpens, R., Zevenhoven-Dobbe, J.C., Laugks, U., Zheng, S., de Jong, A.W.M., Koning, R.I., Agard, D.A., Grunewald, K., Koster, A.J., et al. (2020). A molecular pore spans the double membrane of the coronavirus replication organelle. Science *369*, 1395-1398. 10.1126/science.abd3629.

Wolter, N., Jassat, W., Walaza, S., Welch, R., Moultrie, H., Groome, M., Amoako, D.G., Everatt, J., Bhiman, J.N., Scheepers, C., et al. (2022). Early assessment of the clinical severity of the SARS-CoV-2 omicron variant in South Africa: a data linkage study. Lancet *399*, 437-446. 10.1016/S0140-6736(22)00017-4.

Xu, Z., Shi, L., Wang, Y., Zhang, J., Huang, L., Zhang, C., Liu, S., Zhao, P., Liu, H., Zhu, L., et al. (2020). Pathological findings of COVID-19 associated with acute respiratory distress syndrome. Lancet Respir. Med. *8*, 420-422. 10.1016/S2213-2600(20)30076-X.

Yaniv, K., Ozer, E., Shagan, M., Paitan, Y., Granek, R., and Kushmaro, A. (2022). Managing an evolving pandemic: Cryptic circulation of the Delta variant during the Omicron rise. Science of The Total Environment 836, 155599. https://doi.org/10.1016/j.scitotenv.2022.155599.

Yao, H., Song, Y., Chen, Y., Wu, N., Xu, J., Sun, C., Zhang, J., Weng, T., Zhang, Z., Wu, Z., et al. (2020). Molecular Architecture of the SARS-CoV-2 Virus. Cell *183*, 730-738 e13. 10.1016/j.cell.2020.09.018.

Zhang, J., Cai, Y., Xiao, T., Lu, J., Peng, H., Sterling, S.M., Walsh, R.M., Jr., Rits-Volloch, S., Zhu, H., Woosley, A.N., et al. (2021a). Structural impact on SARS-CoV-2 spike protein by D614G substitution. Science *372*, 525-530. 10.1126/science.abf2303.

Zhang, J., Xiao, T., Cai, Y., Lavine, C.L., Peng, H., Zhu, H., Anand, K., Tong, P., Gautam, A., Mayer, M.L., et al. (2021b). Membrane fusion and immune evasion by the spike protein of SARS-CoV-2 Delta variant. Science *374*, 1353-1360. 10.1126/science.abl9463.

Zhang, K. (2016). Gctf: Real-time CTF determination and correction. J. Struct. Biol. *193*, 1-12. 10.1016/j.jsb.2015.11.003.

Zhang, L., Jackson, C.B., Mou, H., Ojha, A., Peng, H., Quinlan, B.D., Rangarajan, E.S., Pan, A., Vanderheiden, A., Suthar, M.S., et al. (2020). SARS-CoV-2 spike-protein D614G mutation increases virion spike density and infectivity. Nat. Commun. *11*, 6013. 10.1038/s41467-020-19808-4.

Zheng, S.Q., Palovcak, E., Armache, J.P., Verba, K.A., Cheng, Y., and Agard, D.A. (2017). MotionCor2: anisotropic correction of beam-induced motion for improved cryo-electron microscopy. Nat. methods *14*, 331-332. 10.1038/nmeth.4193.

FIGURES

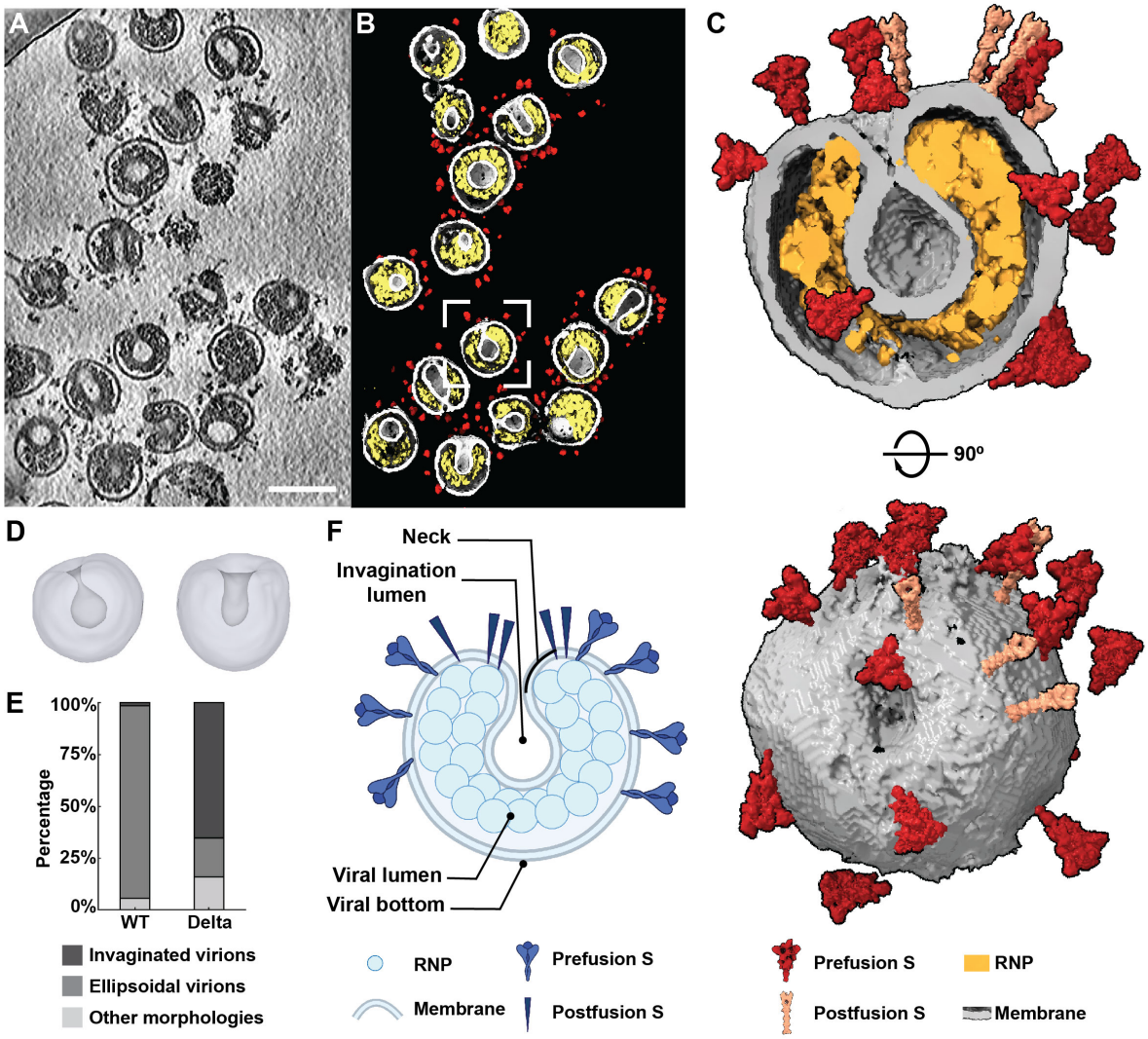

Figure 1. Molecular architecture of SARS-CoV-2 Delta variant.

(A) A representative tomogram slice (5 nm thick) showing pleomorphic SARS-CoV-2 Delta virions. Scale bar: 100 nm. (B) The tomogram in (A) was segmented to distinguish viral spikes (red), membrane (grey) and RNPs (yellow). Each virion in this tomogram harbors an invagination. (C) A topview and slice through a representative invaginated Delta virion showing the prefusion S (red), postfusion S (salmon), lipid envelope (grey) and RNPs (yellow). (D) Two representative types of invagination. One has a balloon-shaped lumen (left), and the other has a cylindrical shaped lumen (right). (E) Percentage of invaginated, ellipsoidal (spherical) and other virion morphologies observed in the WT and Delta virion population. (F) Schematic of an invaginated virion with key parts of the virion named. Created with BioRender.

See also Figures S1 and S2

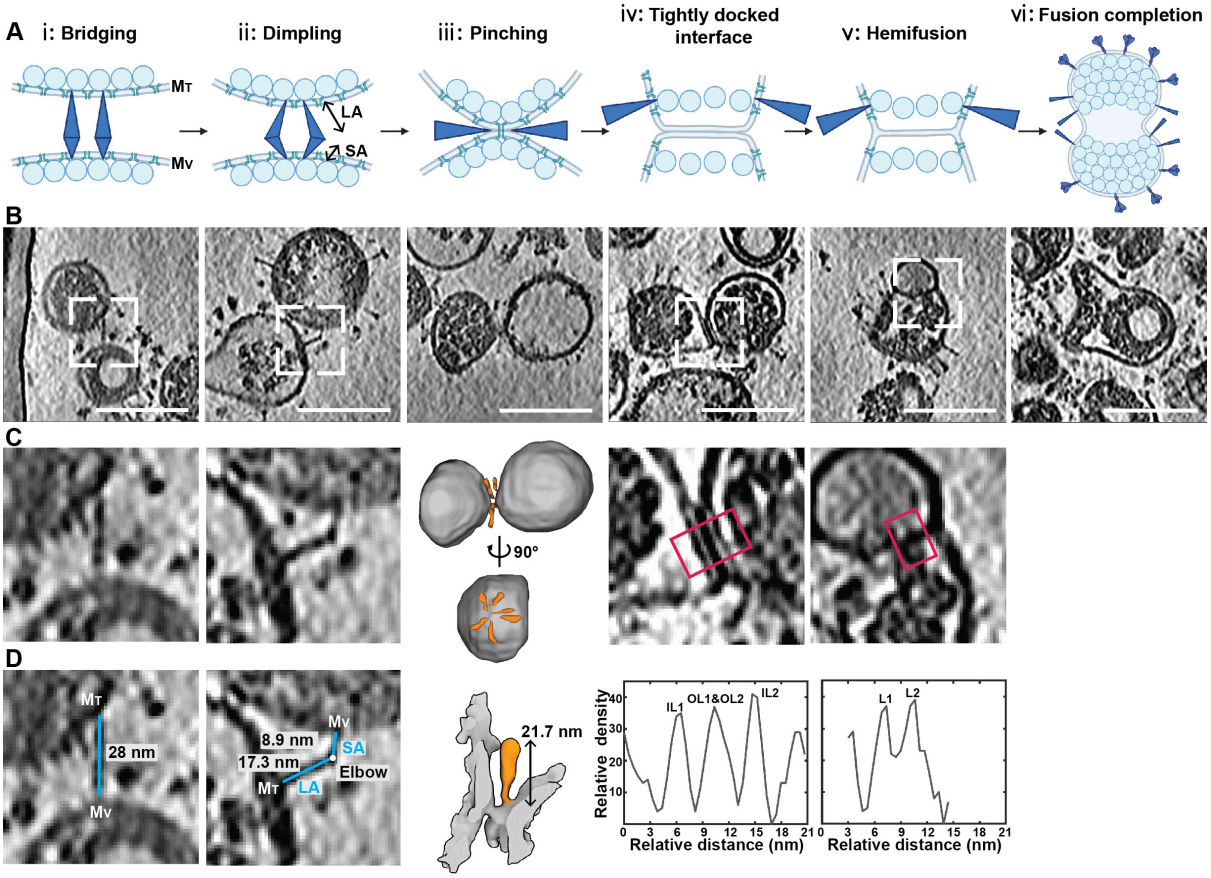

Figure 2. Membrane fusion of SARS-CoV-2 Delta variant.

(A) Observations of intermediate membrane fusion steps were generalized into six stages: i: bridging; ii: dimpling; iii: pinching; iv: tightly docked interface; v: hemifusion and vi: fusion completion. Created with BioRender. (B) Representative tomogram slices (thickness 5 nm, scale bar 100 nm) of the corresponding six fusion stages. (C-D) Characterization of the fusion steps. For the bridging stage, lengths of the bridging spikes were measured. For the dimpling stage, lengths of the shorter arm (SA) and longer arm (LA) of the mediating spikes were measured. For the pinching stage, the tomogram in (B) was segmented. The relative position of the spikes (orange) and the envelope (grey) was shown from the side- and topview. Subtomogram averaging of 15 spikes from 8 independent pinching events shows an S (orange) pinching the envelopes (grey) of two virions. For the tightly docked interface and hemifusion stages, density profiles across the interface (red box) were plot, showing two lipid bilayers (IL: inner leaflet, OL: outer leaflet) for the tightly docked interface and one lipid bilayer (L: leaflet) for the hemifusion stage.

See also Figure S3

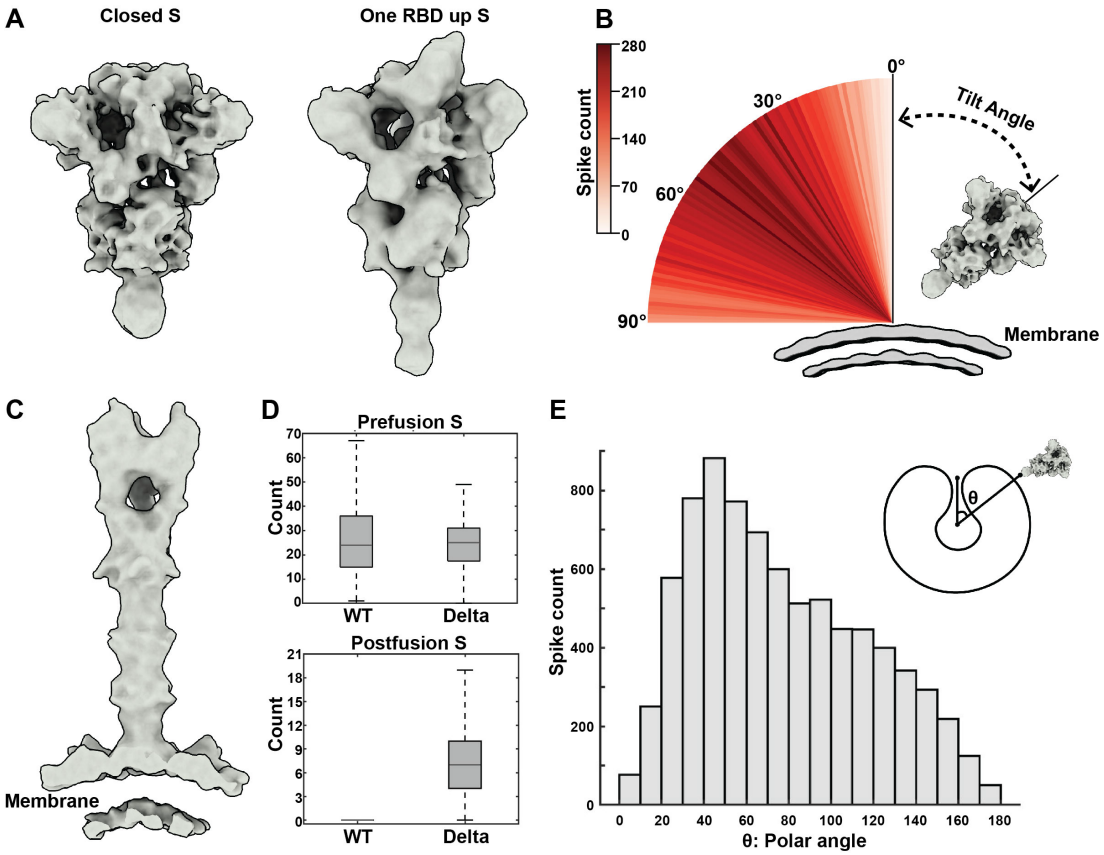

Figure 3. Native structures and distribution of S on the SARS-CoV-2 Delta virion surface.

(A) The native structures of S in the closed and one RBD up prefusion conformations. (B) Distribution of the spike tilt angle reveals a mean tilting angle of 49° (std: 21.5°) relative to the normal axis of the envelope. A representative S in the closed conformation on the envelope is shown. Step size: 1 degree. (C) The native structure of S2 in the postfusion conformation. (D) Statistics on the average number of prefusion (upper) and postfusion (lower) S per virion for the WT and Delta virions. (E) Statistics of S distribution on invaginated virions suggests that the spikes tend to accumulate around the neck area. As shown in the histogram, the invagination direction is defined by the vector from the virion center to the invagination neck; θ, or the spike latitude, defines the angle between the vector from the virion center to the spike stem and the invagination direction.

See also Figure S4

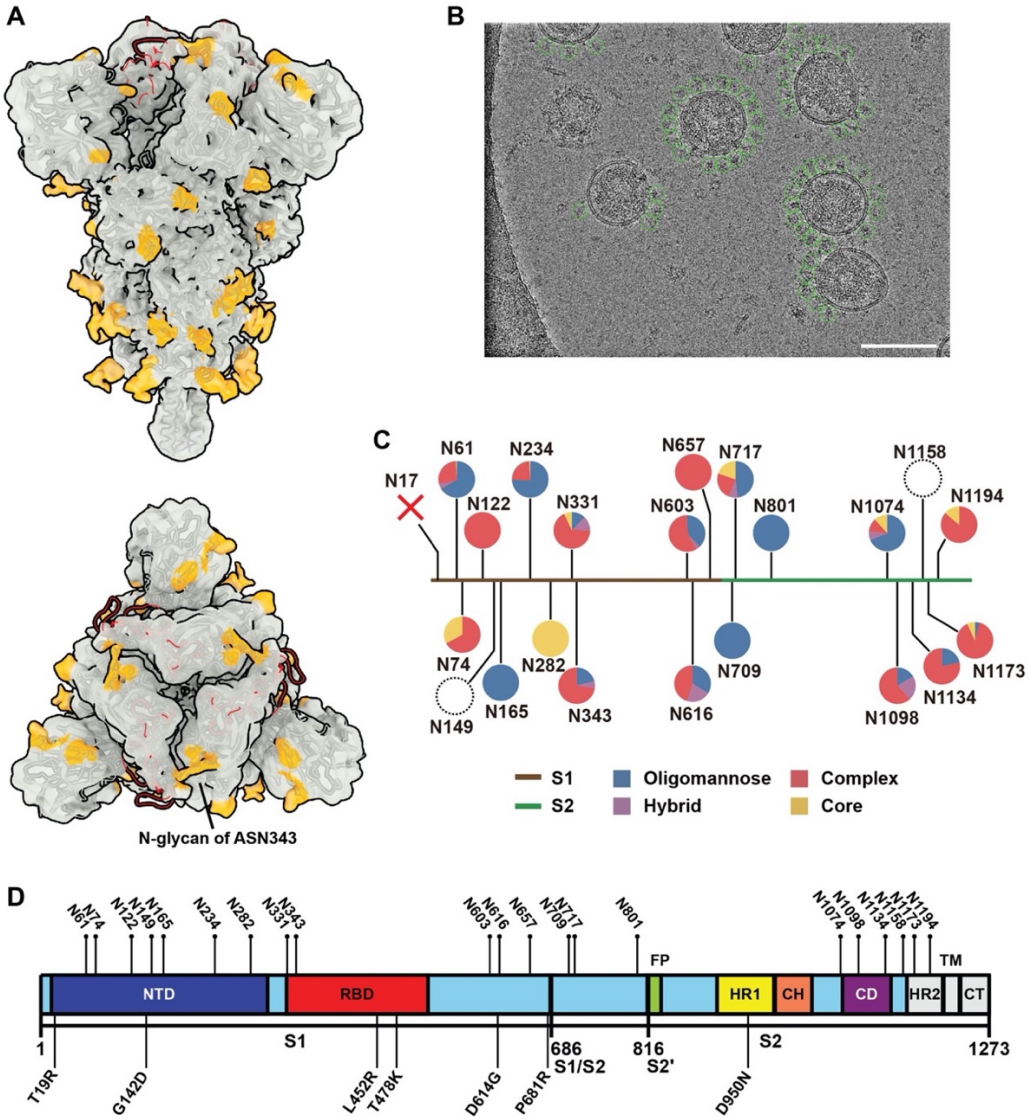

Figure 4. Structure and N-linked glycan composition of native S in the prefusion conformation.

(A) Side- and topview of the native structure of the Delta prefusion S in closed conformation. The structure was determined to 4.13 Å resolution directly from the virion surface by single particle analysis (SPA), fitted with PDB:7SBK and its visible N-linked glycan densities were colored in orange. (B) A cryo-EM micrograph of Delta virions. The identified S in green circles were extracted for SPA. Scale bar: 100 nm. (C) Glycan composition of the native full-length Delta S. The missing glycan N17 due to the mutation was shown as a cross. The undetected glycans N149 and N1158 were shown as dashed circles. (D) Schematic of the Delta S, showing the mutation sites and glycosylation sites. NTD, N-terminal domain; RBD, receptor binding domain; S1/S2, S1/S2 cleavage site; S2', S2' cleavage site; FP, fusion peptide; HR1, heptad repeat 1; CH, central helix; CD, connector domain; HR2, heptad repeat 2; TM, transmembrane anchor; CT, cytoplasmic tail.

See also Figures S5-S7

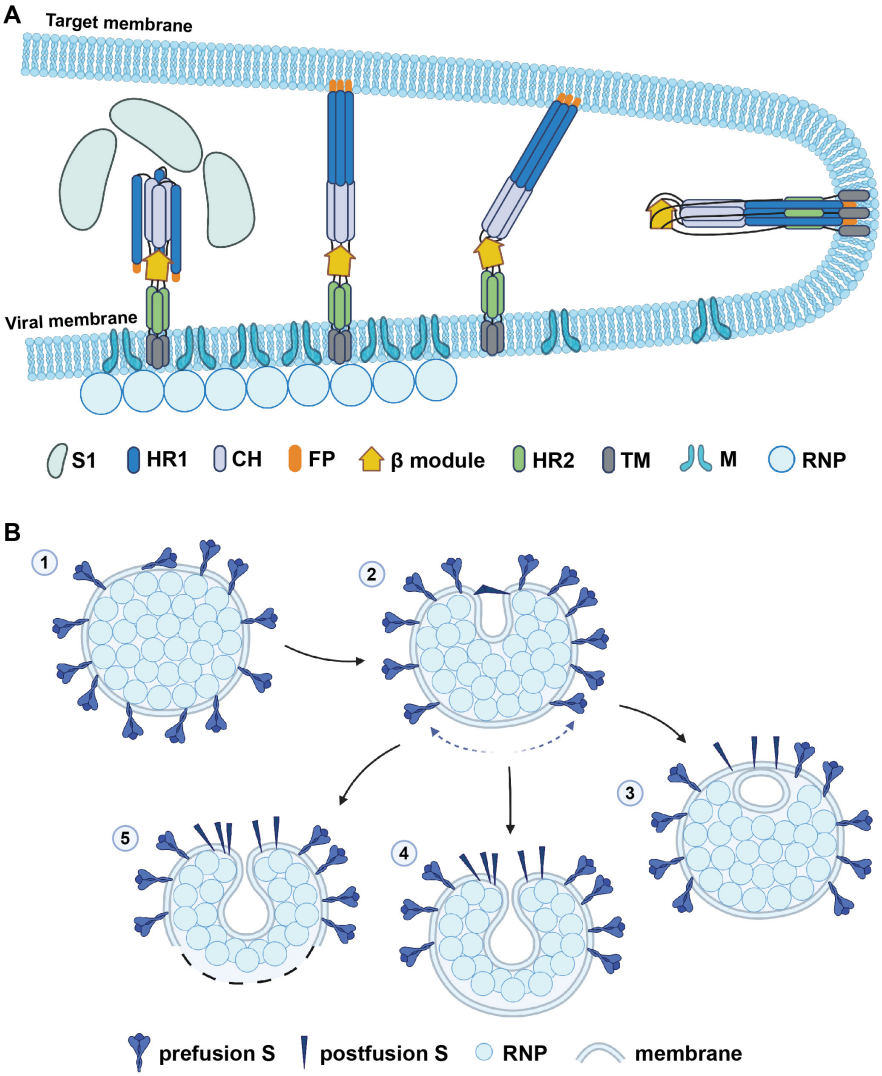

Figure 5. Proposed models for the invagination formation and membrane fusion of SARS-CoV-2 Delta variant.

(A) Model of SARS-CoV-2 S-mediated spontaneous membrane fusion between viral and cellular membranes. S1 spontaneously sheds, then HR1 unfolds and inserts FP into the target membrane, forming an extended intermediate. The FP-HR1-CH region then refolds around the β-module towards the HR2-TM region, pinching the viral- and target membrane. Since this stage, the M- and RNP-lattices have become disrupted and disassembled from the viral membrane. After fusion completion, S2 adopts a postfusion conformation. HR1, heptad repeat 1; CH, central helix; FP, fusion peptide; β module, a β-rich domain (residues 1035-1140); HR2, heptad repeat 2; TM, transmembrane anchor; M, membrane protein; RNP: ribonucleoprotein. (B) Model of the invagination formation in the Delta virion. The invagination is initiated by S lying on the envelope (step 1), followed by a fusion process as shown in (A). S2 wrinkles the membrane to form a dimple, and pulls more S into the fusion event at the neck (step 2). The dimple may be fused into a vesicle (step 3), or enlarged into an invagination. In the latter case, the viral bottom either becomes bald of S and RNPs (step 4), or breaks (step 5). Both models were created with BioRender.

See also Figure S8